Rydberg blockade mechanism through the lens of graph theory: characterization and applications

Elie Bermot, ^{1, 2, *} Lucia Valor, ¹ Wesley Coelho, ¹ Louis-Paul Henry, ¹ and Natalie Pearson ¹ PASQAL, ²⁴ Av. Emile Baudot, ⁹¹¹²⁰ Palaiseau, France ² Université Paris Cité, CNRS, IRIF, Paris, France (Dated: June 17, 2025)

The Rydberg blockade phenomenon is fundamental to quantum algorithms employing neutral atom devices. By preventing two neighboring atoms from being simultaneously excited, it facilitates the embedding of unit disk graphs. This paper provides a comprehensive theoretical analysis of the Rydberg blockade and its behavior under various drive schemes. We introduce new metrics for graph embedding, specifically the correlation matrix and maximum independence violation, and apply them to facilitate the embedding of disk graphs, a parent class of the unit disk graph class. Furthermore, we address the Maximum Independent Set (MIS) problem on embedded disk graphs and demonstrate that a local drive, informed by local blockade radii, outperforms the globally applied drive commonly used for solving the MIS problem in unit disk graphs.

I. INTRODUCTION

In recent years, Rydberg atom quantum computers have become an increasingly popular hardware for implementation of both analog and digital algorithms [1-3]. A key challenge in using neutral atoms for quantum computation is enabling sufficiently strong interactions, which is achieved by exciting them to highly energetic Rydberg levels, thus earning these systems their name. In these highly energetic states, atoms exhibit a much larger electric dipole, allowing them to interact over longer distances. This facilitates twoqubit gates in the digital paradigm [4–6] and is the basis for all interactions in the analog paradigm [7–10]. Typically, the form of this interaction is such that the presence of an atom in a Rydberg state prevents other nearby atoms from being driven into the Rydberg state by shifting the energy of the multiple-excited state. This phenomenon is known as the Rydberg blockade and has been extensively demonstrated in experiment [11-14].

The Rydberg blockade is also used for graph encoding in Rydberg atom arrays, a crucial step in solving combinatorial optimization problems[15–19], or performing quantum graph machine learning algorithms [15, 20–22]. This is usually done by assigning each atom to a node of the original graph, with nodes corresponding to atoms within the blockade range connected by an edge. However, the existing literature documenting this phenomenon does not extend to quantifying the extent of blockade, which may improve encoding implementations, nor is there discussion of the behavior under non-trivial driving scenarios. Considering the broad importance of the Rydberg blockade in neutral atom quantum computing, this motivates our investigation into a more precise characterization and understanding of this effect. Specifically, once graph embedding is performed on the neutral atom device, the Rydberg blockade restricts quantum dynamics to subspaces spanned by states that respect the independent set constraint of the embedded graph, where independent set is a set of non-adjacent nodes. Consequently, we can develop quantum algorithms to find the maximum independent set of the graph [23], which corresponds to identifying the independent set with the maximum cardinality. The types of embeddable graphs are usually limited to the unit disk class, graphs with the property that a pair of vertices is connected by an edge if and only if the Euclidean distance between them is less than or equal to a fixed radius [15, 18, 19]

In this work, we study the main properties of Rydberg blockade in an analog regime under various drive schemes, quantifying the extent of blockade and how this relates to the blockade radius. Further, we extend this to the case of local drive and investigate the implications for graph embedding beyond the previously demonstrated unit disk class. In Section II we develop a metric for blockade, which naturally results in a definition for blockade radius, and use this to determine relationships in three types of driving scenarios for 2 atom systems. Next, in Section III, we extend this to many body systems to report the extent to which these relationships can be generalised and used for graph embedding. Finally, in Section IV, we apply this knowledge to assess the feasibility of using it to find the Maximum Independent Set of graphs beyond unit disk.

II. QUANTIFYING BLOCKADE IN DIFFERENT DRIVE REGIMES

The Rydberg blockade mechanism [12, 24] can be understood through an energy-level representation in the z-basis, where the basis states are the ground state $|g\rangle = |0\rangle$, and a Rydberg state, $|R\rangle = |1\rangle$. In this configuration, the Hamiltonian of a neutral atom system is equivalent to that of a Transverse Field Ising Model (TFIM). With $\hbar = 1$, this takes the form

$$\mathcal{H} = \frac{1}{2} \sum_{i} \Omega_i \sigma_i^x - \sum_{i} \delta_i n_i + \sum_{i < j} \frac{C_6}{r_{ij}^6} n_i n_j, \qquad (1)$$

where r_{ij} is the distance between atoms i and j, $n_i = (1 - \sigma_i^z)/2 = |R\rangle\langle R|$ represents the Rydberg state occupancy of atom i, and σ_i^x is the corresponding Pauli X op-

^{*} elie.bermot@pasqal.com

erator. The parameters $\Omega_i(t)$ and $\delta_i(t)$ correspond to the amplitude and detuning of the laser driving the transition between $|g\rangle$ and $|R\rangle$. The interaction term, characterized by the van der Waals coefficient C_6 , describes the longrange interaction between Rydberg atoms, which scales as $1/r^6$ and depends on the specific Rydberg level targeted. For instance, for a system using the Rydberg state with principle quantum number n = 70, C_6 is $862 \,\mathrm{GHz} \cdot \mu\mathrm{m}^6$, and for n = 82, C_6 is $8870 \,\mathrm{GHz} \cdot \mu\mathrm{m}^6$ [25]. In this project, we use the Rydberg state with principal quantum number n=70. As seen in the last term of Eq. (1), for a pair of atoms, the van der Waals interaction shifts the energy of the doubly excited state $|RR\rangle$ by a factor of C_6/r_{ij}^6 . Assume the atoms are driven by a laser resonant with the $|g\rangle \leftrightarrow |R\rangle$ transition for both atoms ($\delta = 0$). If the atoms are separated by a distance $r \ll r_B = (C_6/\Omega)^{1/6}$, the van der Waals interaction $(C_6/r^6 \gg \Omega)$ shifts the energy of the double excited state $|RR\rangle$ enough, so that it is no longer resonant with the driving laser, and the driving will result in transfer to the entangled state $(|gR\rangle + |Rg\rangle)/\sqrt{2}$.

From this, one can intuitively infer that two atoms are "blockaded" when the dominant energy scale is the interaction shifting $|RR\rangle$, i.e. $\Omega+\delta\ll C_6/r_{ij}^6$, and conversely "non-blockaded" when $\Omega+\delta\gg C_6/r_{ij}^6$. This understanding is used to deduce the distance between atoms i and j within which only one of these atoms may be excited. This distance is generally termed as the "blockade radius" [11, 26] and is usually written as

$$r_B = \left(\frac{C_6}{\Omega + \delta}\right)^{-1/6}. (2)$$

To further characterize the crossover between the block-aded and non-blockaded regimes, we introduce a quantitative measure of blockade strength. A natural choice is the maximum occupation of the doubly excited state over time, defined as $P_{RR} = \max_t |\langle \psi(t)|RR\rangle|^2 \in [0,1]$. For a system driven over a sufficiently long duration, we expect P_{RR} to approach a value of 1 if the atoms are very far apart and the system is free to explore all energetically and symmetrically permitted states, including $|RR\rangle$. If, on the other hand, the atoms are blockaded to some extent, we expect the value of P_{RR} to be bounded above by a quantity related to the extent of the blockade. As such, we quantify blockade as $1-P_{RR}$. With this metric defined we can concretely define the blockade radius to be the distance at which $P_{RR} = 0.5$.

Figure 1(a) depicts three different driving scenarios which we investigate; finding the value of P_{RR} for each of these as a function of the separation between the atoms, $r \equiv r_{12}$, and for various amplitudes, shown in Figure 1(b). Specifically, we study three systems of increasing complexity. The first is a sequentially driven system (labeled S and associated Rydberg blockade radius r_B^S and doubly excited probability P_{RR}^S), where one atom is first excited to $|R\rangle$ and the other is then driven with a constant local amplitude. The second is a simultaneous global system (G, and associated Rydberg blockade radius r_B^G and doubly excited probability P_{RR}^G), in which both atoms start in $|g\rangle$ and are driven simultaneously with the same amplitude. The third

is a simultaneous local system (L, and associated Rydberg blockade radius r_B^L and doubly excited probability P_{RR}^L), where both atoms also start in $|g\rangle$ but are driven simultaneously with different amplitudes.

In the simplest case of sequential drive this is exactly solvable and we find

$$P_{RR}^S(r) = (1 + \left[\Omega^{-1} \left(C_6/r_{ij}^6 - \delta\right)\right]^2)^{-1},$$
 (3)

resulting in a blockade radius, r_B^S identical to that of Eq. (2). For simultaneous global drive this can be computationally solved with a specialized software, such as Wolfram Mathematica [27], resulting in a higher P_{RR}^G for the same values of r and Ω as shown in Fig. 1(b), and therefore resulting in a lower blockade radius r_B^G . The full equation of P_{RR}^G is printed in Appendix A, Eq. (A25). Curiously, we observe that a very good numerical approximation of the resulting blockade radius is $r_B^G = 0.98 r_B^{\hat{S}}$, shown in Fig. 1(c). In the final, simultaneous locally driven system we drive the system with the same average value of the amplitude as in the former driving scenarios $(\Omega = (\Omega_1 + \Omega_2)/2 \in \{1, 3\}$ $\operatorname{rad}/\mu s$), but where the ratio between them is $\Omega_1/\Omega_2=3$. In this case, we cannot solve the system exactly, but we can find a good approximate form for ${\cal P}^L_{RR}$ numerically using a method presented in Appendix B. For this locally driven system, we observe that the corresponding blockade radius r_B^L for this set of amplitudes Ω_i satisfies

$$r_B^L(\Omega_1, \Omega_2) \sim 0.49 \left[r_B^G(\Omega_1) + r_B^G(\Omega_2) \right].$$
 (4)

The simulated and calculated values for r_B are shown in Figure 1(c). Taken together, this provides us with two outcomes. The first is a better way to quantify blockade—this can be useful when embedding graphs in neutral atom quantum systems. The second is a rigorous definition of the blockade radius and its pairwise behavior, most notably in the presence of local drive. In the next sections, we will investigate the implications of using these developments for graph embedding in many body systems.

III. EMBEDDING GRAPHS

Having developed a deeper understanding of the Rydberg blockade phenomenon, we now apply it to optimize graph embedding using the Hamiltonian of a Rydberg atom Quantum Processing Unit (QPU). In particular, by carefully selecting local amplitudes and atom positions, we demonstrate the embedding of a broader class of graphs using our methods, namely disk graphs [28]. A disk graph is a type of geometric graph where each vertex represents a the center of a disk in the Euclidean plane, and edges are drawn between vertices if and only if the corresponding disks overlap. If all radii are equal, this reduces to a unit disk graph. Here, we propose a new method to deterministically embed disk graphs in order to solve combinatorial optimization problems on them in the next section.

To test this disk graph embedding strategy, we perform a quench $|\psi(T)\rangle$ of duration $T=100\mu s$ using the QPU

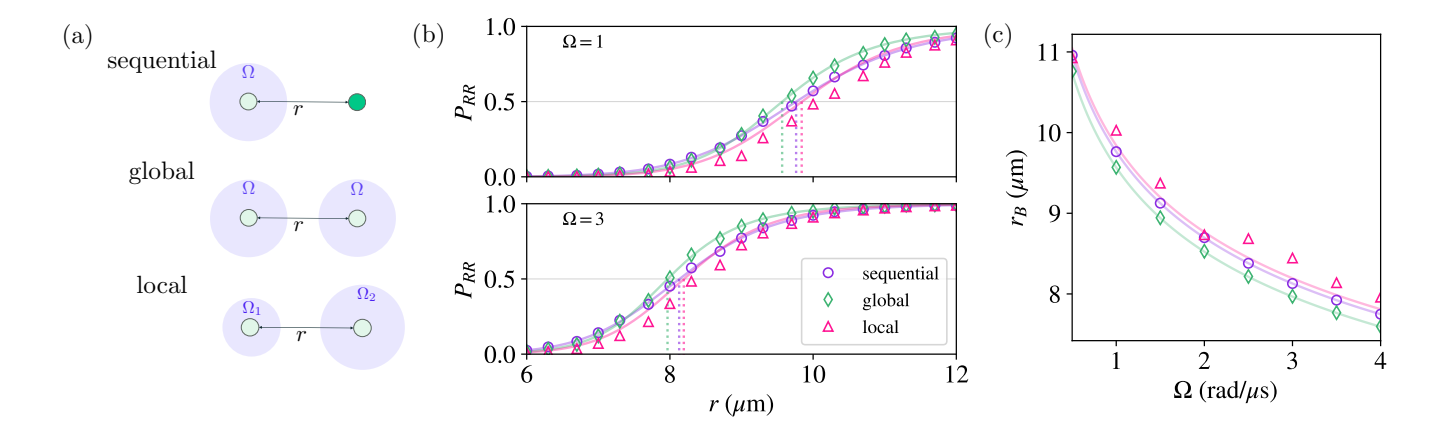


Figure 1. (a) The three driving scenarios are illustrated, where the light (dark) green circles correspond to atoms initialized in the ground (excited) state and driven with lasers with amplitudes Ω . (b) The maximum probability of measuring both atoms in the Rydberg state during a quench with average amplitudes 1 rad/ μ s (upper) and 3 rad/ μ s (lower) for each driving scenario. Markers indicate simulated results over 50μ s, solid lines are calculated using the equations mentioned in the main text. Dotted lines show where the calculated values cross $P_{RR} = 0.5$ and hence define the blockade radius r_B . (c) The simulated (markers) and calculated (solid lines) values of r_B for a range of amplitudes. For the locally driven case the average amplitude is Ω and the ratio is $\Omega_2/\Omega_1 = 3$

Hamiltonian of Eq. (1), under two configurations. The first is a global pulse with amplitude $\Omega=0.98C_6/r_B^6$, corresponding to the Rydberg blockade radius for the unit disk graph; the second is a scheme of local amplitudes $\Omega_i=0.98C_6/r_{B,i}^6$, corresponding to the local Rydberg blockade radii. The resulting final states encode the target graph structures according to the blockade behavior described in previous sections and shown in Figure 2.

To evaluate the quality of the embedding, we characterize the graphs based on their independent set properties. Let us recall that, for a given graph G=(V,E), an independent set is a subset $S\subseteq V$ such that no two vertices in S are connected, i.e., $\forall u,v\in S, (u,v)\notin E$. We define the maximum independence violation probability as the maximum value of the expectation value of the projector onto the subspace of non-independent sets over all t during the quench,

$$P_{\text{violation}} = \max_{t} \langle \psi(t) | \Pi_{\text{non-independent}} | \psi(t) \rangle,$$
 (5)

where $\Pi_{\text{non-independent}}$ projects onto states that do not form an independent set. This metric reduces to P_{RR} for the two atom case, assuming the two atoms share an edge. We repeat this for different distance scales by scaling the atomic coordinates by a parameter λ . By assuming the same underlying graph, we expect that, for some λ , atoms will be too distant for their interaction to well implement an edge between them. We refer to this as the 'breaking' of an edge, and define a critical value of the scaling λ_c to be the value at which the first edge is broken. The behavior of λ_c differs between unit disk graphs and disk graphs. For unit disk graphs, λ_c corresponds to the point where the maximum separation between connected atoms exceeds the blockade radius. In contrast, for disk graphs, edges can break between atom pairs that are not necessarily the furthest apart, since blockade radii vary. For $\lambda < \lambda_c$, the maximum independence violation should be minimal, as all atoms remain blockaded. However, for $\lambda > \lambda_c$, at least one expected edge in the embedded graph may be missing. Therefore, we expect the mean independence violation probability to exhibit a behavior similar to P_{RR} , as described in the previous section.

This encoding is further studied by looking at the maximal correlation matrix, defined as

$$C_{ij} = \max_{t} \langle \psi(t) | n_i n_j | \psi(t) \rangle.$$
 (6)

A small value of C_{ij} implies that atoms i and j cannot be excited at the same time, while a large value implies that both atoms can be. Therefore, if the maximum independence violation is small, it is expected to also have a small value of the maximal correlation matrix between connected edges. Conversely, a large maximum independence violation value is expected to correspond to a large correlation matrix value across connected edges.

As shown in Figure 2, we consider a star-like arrangement of atoms and two resulting graphs (one unit disk and one disk), generated by setting a global Rydberg blockade radius r_B in the unit disk case and modifying the radii on atoms 0, 4, and 5 in the disk graph case. We choose the global blockade radius $r_B = 7.9055, \mu \text{m}$ such that it corresponds to an amplitude of $\Omega = \pi \operatorname{rad}/\mu s$, and the modified radii, $r_{B,c} = 13.0247 \mu \text{m}$, such that the amplitude becomes $\Omega_i = \pi/20 \text{ rad}/\mu \text{s}$ for the corresponding atoms. Atoms are arranged with a uniform separation of $0.9r_B$. We analyze three driving protocols: (i) a global pulse applied to the unit disk graph, (ii) a local pulse applied to the disk graph, and (iii) a local drive with randomly shuffled amplitude radii, also applied to the disk graph, to act as a control case. In the global protocol, the amplitude is uniform across all atoms and given by $\Omega = \pi$. In the local protocol, local amplitudes are used to implement local blockade

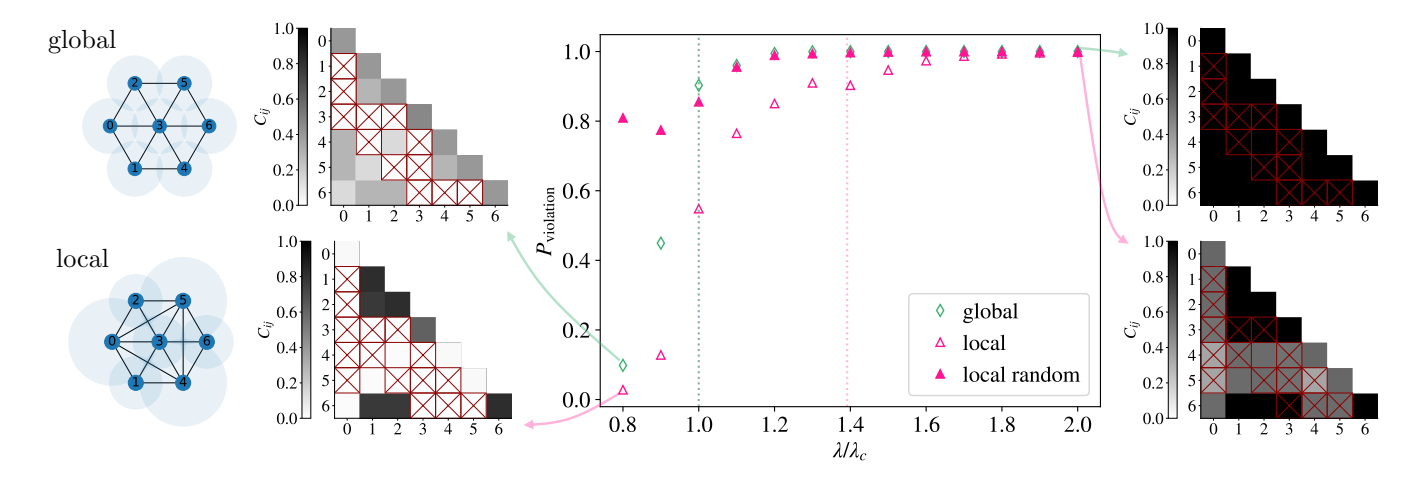


Figure 2. Graph embeddings for unit disk graphs (top) and disk graphs (bottom) are evaluated using correlation matrices and maximum independence violation metrics. Both graphs have the same atom position, but local radii result in different connectivity. The radii, $r_{B,i} = 0.98 \, ^6\!\!\!\!\! / \, C_6/\Omega_i$, are implemented using a global drive of $\Omega_i = \pi$ for the unit disk graph (green open diamonds) or a local drive with $\Omega_i = \pi/20$ for $i \in (0,4,5)$ for the disk graph (pink open triangles). A local drive implementation using the same set of local amplitudes but applied to random atoms (pink filled triangles) is shown as a control. A 100μ s quench is performed with the atomic register scaled by λ , where $\lambda = \lambda_c$ (black dotted line) is the point at which the first edge in the graph is expected to break. Full disconnection of the unit disk graph also occurs at this point, whereas full disconnection of the disk graph is shown by the pink dotted line. The maximum correlation matrix is measured at connected $(\lambda/\lambda_c = 0.8)$ and disconnected $(\lambda/\lambda_c = 2)$ scaling values, and overlapped by red crosses which indicate edges in the graph.

radii; $\Omega_i = \pi/20$ for atoms 0, 4, and 5, and $\Omega_i = \pi$ for all others. In the randomly shuffled protocol, each atom i is independently assigned a local amplitude $\Omega_i = \pi/20$ with probability 3/7, and $\Omega_i = \pi$ otherwise. Figure 2 shows both the maximum independence violation as a function of the scaling parameter λ/λ_c for the global, local, and randomly shuffled driving protocols, and the corresponding correlation matrices for small and large values of this ratio, in the former two cases. In the correlation matrices, red squares with diagonal crosses denote edges present in the encoded graph. For $\lambda < \lambda_c$ (to the left of the black dotted line), independence is expected to be preserved. This is confirmed for both the global (green diamonds) and local pulses (pink unfilled triangles), where the maximum independence violation remains below 0.2. In contrast, the randomly shuffled protocol (pink filled triangles) exhibits significantly larger maximum independence violations, around 0.8, indicating a breakdown of independence. In this regime, the correlation matrix elements $\langle n_i n_j \rangle - \langle n_i \rangle \langle n_j \rangle$ corresponding to edges in both the unit disk and disk graphs remain near 0, consistent with the Rydberg blockade phenomenon. Notably, the disk graph includes three additional edges (0-4, 0-5, and 4-5) relative to the unit disk graph, yet these also show low correlations in the presence of the local drive designed to encode them, confirming that independence is maintained even for these added connections. For larger λ/λ_c (e.g., $\lambda/\lambda_c=2$), atoms are spaced farther apart, making double excitations more likely as the conditions for edge encoding are violated. Accordingly, the maximum independence violation approaches 1 across all protocols, and the structure of the correlation matrices changes, with many entries increasing beyond 0.2. These observations demonstrate that both the maximum independence violation metric and the correlation matrix can be used to assess how faithfully a given graph has been encoded. In the locally driven case, although we observe pairwise independence as expected, we also sometimes observe it when unexpected, as seen by the presence of low correlation values for some unconnected pairs, for $\lambda/\lambda_c = 0.8$. In this case, we have restricted the system to the independent manifold as desired. An ideal embedding would have explored this manifold uniformly, so that all elements of C_{ij} not corresponding to an edge would be of similar values.

IV. COMBINATORIAL OPTIMIZATION PROBLEMS

A prominent application of Rydberg platforms is ground state preparation via quantum annealing, for solving combinatorial optimization problems [29–31] such as the Maximum Independent Set (MIS) problem. The MIS problem involves finding the largest independent set in a given graph G. Quantum annealing achieves this by initializing the system in the known ground state of a simple Hamiltonian. Then, by gradually transforming it into a Hamiltonian which encodes the MIS problem, the adiabatic theorem [32] ensures the system remains in its ground state, thereby evolving into a state representing the MIS solution, obtained with a Pauli-Z measurement.

Given a graph G = (V, E), the Hamiltonian which encodes the MIS problem can be written as:

$$H_{MIS} = -\sum_{i \in V} n_i + U \sum_{(i,j) \in E} n_i n_j,$$
 (7)

where each vertex $i \in V$ corresponds to a qubit, and where

qubits measured in the Rydberg state after annealing represent the vertices in the MIS. The first term energetically rewards the excitation of atoms, and hence the presence of vertices in the set. Choosing $U\gg \Delta(G)$ in the second term, where $\Delta(G)$ is the graph's maximum degree, makes it energetically expensive for neighboring vertices to both occupy the state $|R\rangle$. This ensures low-energy states correspond to MIS solutions.

In Rydberg atom devices [19, 33, 34] with Hamiltonian \mathcal{H} as in Eq. (1), the MIS problem can be encoded by setting $\Omega=0$ and choosing atom positions and detuning δ in order to match Eq. (7) as closely as possible. This approach has been effectively demonstrated for unit disk graphs with common embedding strategies [15, 19]. Extensions to more complex graph classes have been achieved either by introducing a large resource overhead—through increasing the number of atoms [35, 36]—or by using variational methods [37].

So far we have shown that driving atoms individually with finite, local amplitudes provides them with local blockade radii. This motivates us to investigate whether our deterministic method for embedding disk graphs can also be used within annealing algorithms, for solving the MIS problem beyond unit disk graphs [28, 38]. We do this by studying the ground-state properties of the Rydberg system after annealing with local, finite amplitudes Ω_i (in contrast to the usual $\Omega=0$). It should be noted that the introduction of finite drive as part of the graph encoding shifts the eigenstates of the Hamiltonian away from the Pauli-Z basis, so measurements in this basis become projective.

To study the impact of such local drive configurations, we compared the probability of measuring a MIS on disk graphs and unit disk graphs for a problem Hamiltonian with both local and global, finite drives. The problem Hamiltonian used, $\mathcal{H}(\kappa, \delta_f)$, is that of Eq. (1), where we choose local amplitudes to encode the desired disk graph $\Omega_i = \kappa C_6/r_{B,i}^6$ and a global detuning δ_f . The global drive is defined equivalently, but with all radii set to the average value $\Omega = \kappa C_6/r_{B,\text{avg}}^6$, where $r_{B,\text{avg}} = N^{-1} \sum_{i=1}^N r_{B,i}$. For a given graph type, the probability of measuring the MIS at the end of the annealing schedule is

$$P_{\Gamma}^{dr}(\kappa, \delta_f) = \sum_{\{\text{MIS}(\Gamma)\}} |\langle \text{MIS}(\Gamma)|\psi_0^{dr}(\kappa, \delta_f)\rangle|^2, \qquad (8)$$

where $dr \in \{l, g\}$ indicates the local or global drive, $\Gamma \in \{UD, D\}$ indicates a disk or unit disk graph, and $|\psi_0^{dr}(\kappa, \delta_f)\rangle$ is the ground state of $\mathcal{H}(\kappa, \delta_f)$ under the respective driving configuration.

The maximum MIS probability for each graph type and drive is found by optimal choice of κ and δ_f ,

$$P_{\Gamma}^{dr} = \max_{(\kappa, \delta_f)} P_{\Gamma}^{dr}(\kappa, \delta_f). \tag{9}$$

In order to quantify how much improvement we have obtained through use of local drive for encoding we define the relative improvement ratio

$$R(\Gamma) = \frac{P_{\Gamma}^L - P_{\Gamma}^G}{P_{\Gamma}^G},\tag{10}$$

where $R(\Gamma) > 0$ indicates that the schedule using local drive performed better than with global drive, while $R(\Gamma) < 0$ implies the opposite.

For each system size N, we generated 40 random instances of disk graphs defined by local Rydberg blockade radii $\{r_{B,i}\}_{i=1}^{N}$. As control, we generate corresponding unit disk graphs by averaging the local radii, yielding a uniform blockade radius $r_B = N^{-1} \sum_{i=1}^{N} r_{B,i}$. Under local drives, we expect disk graphs to potentially perform better, due to the embedding strategy. However, unit disk graphs should perform worse, since the local drives and the blockade radii (now uniform) become mismatched.

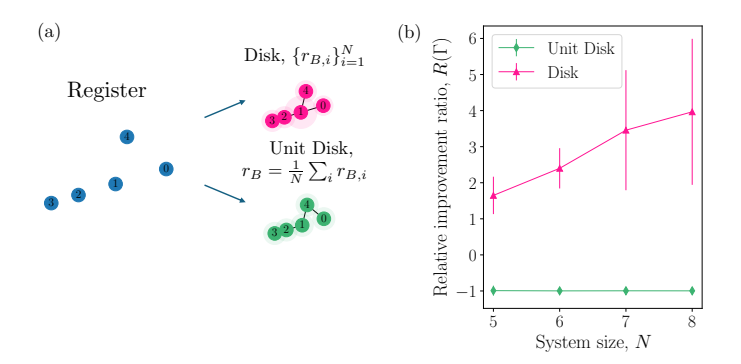


Figure 3. (a) Given an example instance for an atomic register of size N (left), one can generate a disk graph (top) with local blockade radii $\{r_{B,i}.i=1^N, \text{ chosen randomly.} \text{ The corresponding unit disk graph is obtained by averaging the values of } \{r_{B,i}\}_{i=1}^N$. (b) Relative improvement ratio $R(\Gamma)$ for disk graphs (pink triangles) and their associated unit disk graphs (green diamonds) across different system sizes. Each $P_{\text{MIS}}(G)$ is computed by finding the optimal values of parameters determining the problem Hamiltonian $H(\kappa, \delta_f)$. Each point represents the median improvement ratio over 40 random graphs, with error bars indicating 90% confidence intervals. $R(\Gamma)$ is positive for disk graphs, thus showing that driving locally increases performance, as compared to using a global drive. The opposite is true for, unit disk graphs, which yield $R(\Gamma) \approx -1$.

An example of the graph generation process is shown in Figure 3(a), with further details provided in Appendix C. Figure 3(b) displays the median and 90% confidence intervals of the relative improvement ratio $R(\Gamma)$, for both disk and unit disk graphs. The parameters (κ, δ_f) were optimized to maximize the success probability P_{Γ}^{dr} under each drive configuration. The results demonstrate that the use of local drives significantly improves the MIS success probability on disk graphs, with consistently positive values of $R(\Gamma)$ across all system sizes. For a representative graph instance at N=5, the local setting yielded a success probability of $P_D^l=0.12$, compared to $P_D^g=0.05$ for the global setting, corresponding to a relative increase by a factor of 2.4. In contrast, for the associated unit disk graph, the local success probability was $P_{UD}^l=9.95\times 10^{-5}$,

while the global value was $P_{UD}^g=0.04$, indicating that the local drive configuration fails to identify the MIS within this framework. Furthermore, $R(\Gamma)$ increases with system size, suggesting even more favorable results for local drives in larger systems. In contrast, for unit disk graphs, $R(\Gamma)$ remains approximately constant and close to -1. As expected, this indicates that a global drive is favorable for the unit disk graph case. These findings suggest a useful application of our deterministic embedding methods using local drives, enabling MIS search beyond unit disk graphs.

V. CONCLUSION AND OUTLOOK

In this work, we proposed and studied a theoretical definition of the Rydberg blockade phenomenon under various types of drives. After quantifying blockade in each of these drive types, we utilized the findings to embed a broad class of disk graphs, which can be employed in various applications such as for optimization problems like the MIS problem [33]. We proposed and tested a method to solve the MIS problem for this class of graphs using local amplitude and projective measurements, and compared it favorably to a set of control cases of unit-disk graphs with the same average disk radii.

We demonstrated the utility of this deterministic embedding ability for solving the MIS problem in disk graphs using quantum annealing. This method differs from the standard protocol by its use of finite drive, and thus requires projective measurements, but showed promising improvement in solution probabilities for the disk graphs tested.

The many body implementation of this embedding remains qualitative, and would benefit from further study in order to quantitatively assess its effectiveness in useful applications. Experimental challenges in annealing to a state with a finite drive may limit the feasibility of the specific MIS algorithm suggested. The extent to which the projective measurement requirement reduces the efficiency also warrants further investigation.

Appendix A: Analytical description of the 4 level system for a global simultaneous drive

We can diagonalise the Hamiltonian of the two-atom globally driven system with minimal approximation, from which we can obtain the occupation of the doubly-excited state. Although directly differentiating the resulting expression is not achievable, we are able to obtain an expression for the full analytic solution for P_{RR} , for any given r, Ω and δ .

Let us rename our variables as $A = -\delta$, $B = \Omega/2$, $C = (C_6/r^6) - 2\delta$. Then, we can write \mathcal{H} in matrix form as

$$\mathcal{H} = \begin{pmatrix} 0 & B & B & 0 \\ B & A & 0 & B \\ B & 0 & A & B \\ 0 & B & B & C \end{pmatrix}. \tag{A1}$$

To quantify how blockaded a pair of atoms is, we can

study the maximum "leakage" onto the $|RR\rangle$ state, that is, the peak population of $|RR\rangle$ after evolving the system for a long time. This can be found by calculating $\langle RR|U(t)|\psi_0\rangle$, where $|\psi_0\rangle$. We can write $|\psi_0\rangle$, U(t) and $|RR\rangle$ in terms of our system's eigenstates and eigenvalues,

$$|\psi_0\rangle = \sum_i \lambda_i |\psi_i\rangle, \quad U(t) = \sum_i e^{-iE_i t} |\psi_i\rangle\langle\psi_i|, \quad (A2)$$

$$|RR\rangle = \sum_{i} \beta_i |\psi_i\rangle.$$
 (A3)

With this, we can extract out the element in U(t) which takes us from our initial state to $|RR\rangle$ as

$$U_{RR} = \langle RR|U(t)|\psi_0\rangle \tag{A4}$$

$$= \sum_{i,j,k} e^{-iE_j t} \lambda_i \beta_k \langle \psi_k | \psi_j \rangle \langle \psi_j | \psi_i \rangle \tag{A5}$$

$$= \sum_{i} e^{-iE_i t} \lambda_i \beta_i. \tag{A6}$$

The population of $|RR\rangle$ is then $U_{RR}U_{RR}^*$. Here, it is important to note that all of the entries in \mathcal{H} are real, and hence all λ_i , β_i will be real. With this,

$$(U)_{RR}(U^*)_{RR} = \left[\sum_{i} e^{-iE_i t} \lambda_i \beta_i\right] \left[\sum_{j} e^{-iE_j t} \lambda_j \beta_j\right]^*$$

$$= \sum_{i} (\lambda_i \beta_i)^2 + 2 \sum_{i>j} (\lambda_i \beta_i)(\lambda_j \beta_j) \cdot \cos(\Delta E_{i,j} t).$$
(A8)

Now, we can use the property that, for two periodic functions f(x) and g(x) with periods a and b, respectively, the period of f(x)+g(x) will be the least common multiple between a and b. This means that $\sum_{i>j}\cos(\Delta E_{i,j}t)$ will (at least, approximately) saturate at 1 for a long enough time. Then, we can reduce the above equation to

$$(U)_{RR}(U^*)_{RR}^{\max} = \sum_{i} (\lambda_i \beta_i)^2 + 2 \sum_{i>j} |(\lambda_i \beta_i)(\lambda_j \beta_j)|. \quad (A9)$$

The eigenvectors of our Hamiltonian can be written as follows,

$$v_{1} = (0, -1, 1, 0)$$

$$v_{i} = \left(\frac{E_{i} - C}{E_{i}}, \frac{E_{i} - C}{2B}, \frac{E_{i} - C}{2B}, 1\right)$$
 for $i = 2, 3, 4,$
(A11)

so, for example, if we start with our system in the double ground state, $|gg\rangle$, we will have

$$(UU^*)_{|RR\rangle\langle gg|}^{\max} = \sum_{i=2} \left(\frac{E_i - C}{E_i} \cdot \frac{1}{L_i^2} \right)^2$$

$$+ 2 \sum_{i>j=2} \left| \left(\frac{E_i - C}{E_i} \cdot \frac{1}{L_i^2} \right) \left(\frac{E_j - C}{E_j} \cdot \frac{1}{L_j^2} \right) \right|.$$
(A12)
$$(A13)$$

where L_i is the length of vector i, i.e.,

$$L_i = \sqrt{\left(\frac{E_i - C}{E_i}\right)^2 + 2 \cdot \left(\frac{E_i - C}{2B}\right)^2 + 1}$$
 (A14)

The eigenvalues can be written as follows,

$$E_2 = \frac{1}{3} \left(A + C - 2\sqrt{P} \cdot \cos\left(\frac{\tan^{-1}(Q/M)}{3}\right) \right) \quad (A15)$$

$$E_3 = \frac{1}{3} \left(A + C + \sqrt{P} \cdot \cos\left(\frac{\tan^{-1}(Q/M)}{3}\right) \right)$$
 (A16)

$$-\sqrt{3P} \cdot \sin\left(\frac{\tan^{-1}(Q/M)}{3}\right)$$
 (A17)

$$E_4 = \frac{1}{3} \left(A + C + \sqrt{P} \cdot \cos\left(\frac{\tan^{-1}(Q/M)}{3}\right)$$
 (A18)

$$+\sqrt{3P}\cdot\sin\left(\frac{\tan^{-1}(Q/M)}{3}\right)$$
, (A19)

where,

$$P = -3AC + 12B^2 + (A+C)^2$$
(A20)

$$M = 27B^{2}C + \frac{9}{2}(A+C)(AC-4B^{2}) - (A+C)^{3}$$
 (A21)

$$Q = \sqrt{P^3 - M^2} \ . \tag{A22}$$

We observe that, for $\delta=0$, for all three systems, P_{RR} is symmetric around the value 0.5, i.e. around r_B . Motivated by this, and with the goal of writing a more simple expression to well approximate $P_{RR}^{\rm G}$ (i.e. P_{RR} for the global system) we translate the sequential (global) curve by $r_B(r_B^{\rm G})$ and scale by a factor $\Delta^\pi(\Delta^{\rm G})$, defined that the gradient at $r=r_B(r_B^{\rm G})$ is 1. We determine the value of Δ^π analytically and that of $\Delta^{\rm G}$ numerically using the expression for $P_{RR}^{\rm G}$. The resulting gradients are

$$\Delta^{\pi} = \frac{\partial P_{RR}^{\pi}}{\partial r} \bigg|_{r=r_B^{\pi}} = \frac{3}{r_B^{\pi}}$$

$$\Delta^{G} = \frac{\partial P_{RR}^{G}}{\partial r} \bigg|_{r=r_B^{G}} = \frac{3.864}{r_B^{\pi}},$$
(A23)

and can be used to map the global curve onto the sequential one by mapping the atom separation r as follows

$$r \to \frac{\Delta^{\mathrm{G}}}{\Lambda^{\pi}} (r - r_B^{\mathrm{G}}) + r_B^{\pi}.$$
 (A24)

With this we can write a much simplified expression for P_{RR}^G ,

$$P_{RR}^{G} = \frac{1}{1 + \left[\frac{1}{\Omega} \cdot \left(\frac{C_6}{(1.29r - 0.26r_B)^6}\right)\right]^2},$$
 (A25)

Appendix B: Locally driven blockade radius

For locally driven systems we restrict ourselves for simplicity to the zero detuning case with Hamiltonian

$$\mathcal{H} = \frac{1}{2} \sum_{i} \Omega_i \sigma_i^x + \sum_{i \neq j} \frac{C_6}{r_{ij}^6} n_i n_j,$$
 (B1)

which, even for a 2 atom system is nontrivial to diagonalise. As a result we cannot solve the Schrödinger equation to find an analytic expression for the maximum occupation of the doubly-excited state as we did for the sequential and global systems. Instead, we use the same observation of near-symmetry as when building a simplified expression for global simultaneous driving system to find $P_{RR}^{\rm L}$ (i.e. P_{RR} for the local system) by rescaling r and using the simple expression for P_{RR}^{π} . This requires an expression for $r_B^{\rm L}$ (respectively) to implement

$$r \to (\Delta^{\mathcal{L}}/\Delta^{\pi}) \cdot [r - r_B^{\mathcal{L}}] + r_B^{\pi}.$$
 (B2)

The blockade radius r_B^L is found by choosing a symmetric expression across both atoms which obeys the value found using the global system) for $\Omega_0 = \Omega_1$ to match,

$$r_B^{\rm L} = \frac{1}{2} \left(r_{B,0}^{\rm G} + r_{B,1}^{\rm G} \right),$$
 (B3)

where $r_{B,i}^{G}$ is the blockade radius one would expect from a globally driven system with amplitude Ω_i . We compare this to values found from simulated data for different Ω_0 . Ω_1 values, in Figure 4, using simulations sampling from a restricted set of distances around the expected value of r_B^L , such that a high resolution in r can be achieved. For all simulations in this section we evolve for $15\mu s$. Using simulation to obtain P_{RR} values through can result in lower values being obtained than the true maximum values, if the pulse duration used is not sufficient to reach the maximum. This leads to larger inferred values of the blockade radius than accurate. As such, we expect that Eq. (B3) to set the lower bound for the simulation-inferred values of r_B^L , as seen in Figure 4. Data points with lower Ω_1/Ω_0 were rarely satisfied the criteria used to ensure good approximation, so we restrict the ratio range to $\Omega_1/\Omega_0 \in [0.4, 1]$.

It is clear from Eq. (B3) that we could instead use the global expression for the pairwise blockade radius and instead consider an effective amplitude of the local system to be the generalized mean of the two amplitudes with exponent -1/6, $\Omega_{\rm eff} = \left(\frac{1}{2}[\Omega_0^{-1/6} + \Omega_1^{-1/6}]\right)^{-6}$.

We repeat the process of finding a gradient $\Delta^{\rm L}$ using simulation results by applying the rescaling described in Eq. (B2) to simulated data over a range of distances (5-24.75 μ m) and finding value of $\Delta^{\rm L}$ which minimises the least-squares difference between P_{RR}^{π} and the rescaled $P_{RR}^{\rm L}$. This was repeated for 61 combinations of Ω_0 and Ω_1 and the resulting values of $\Delta^{\rm L}$ are shown as a function of $1/r_B(\Omega = \Omega_{\rm eff})$ in Figure 5. We then fit to these data

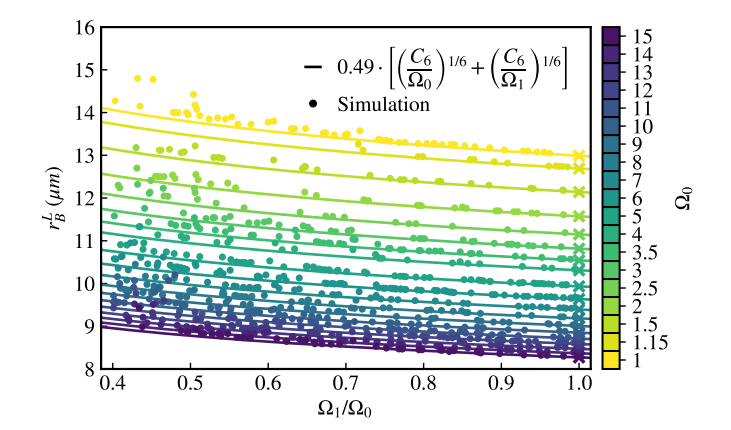


Figure 4. Blockade radius for systems with local simultaneous drive with different Ω_0 and Ω_1 , obtained by simulation (circular points). Pulse durations for each simulation were chosen differently. Crosses mark data points where $\Omega_0 = \Omega_1$ and solid lines indicate the value of $r_B^{\rm L}$ found using Eq. (B3).

points to find the relation

$$\Delta^{\rm L} = \frac{\partial P_{RR}^{\rm L}}{\partial r} \bigg|_{r=r_B^{\rm L}} = \frac{3.475}{r_B^{\pi}(\Omega = \Omega_{\rm eff})}.$$
 (B4)

For a small number of the simulations we observe large fluctuations of $P_{RR}^{\rm L}$ at random values of r, despite the expectation that the function is monotonic. We attribute a higher error to simulations with larger fluctuations and these errors are then taken into account in the fitting procedure in Figure 5, where data points with larger fluctuations contributing less to the fit. The 'fluctuability' of each simulation was calculated by tracking the changes in $P_{RR}^{\rm L}$ within non-monotonic regions of the data. This fluctuability was considered when fitting the data points to a linear function, where the fit is found by minimizing $\sum_i d_i \cdot (1-F_i)$, where d_i is the distance between data point i and the fit, and F_i is the fluctuability of point i.

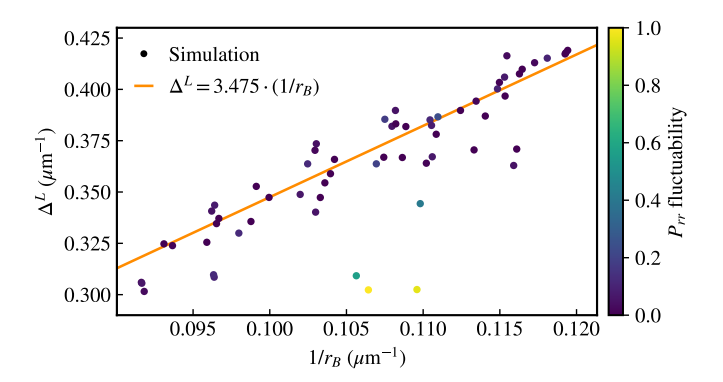


Figure 5. Gradient for systems with local simultaneous drive obtained by minimizing the distance from Eq. (3) to simulated data, shifted and rescaled according to $r \to (\Delta^{\rm L}/\Delta^{\pi}) \cdot [r - r_B^{\rm L}] + r_B^{\pi}$. Points of higher fluctuability are shown lighter.

This enables us to write

$$P_{RR}^{L} = \frac{1}{1 + \left[\frac{1}{\Omega_{\text{eff}}} \cdot \left(\frac{C_6}{(1.18r - 0.16r_B)^6}\right)\right]^2},$$
 (B5)

which is plotted in Figure 6 (a) for five of the studied simulations and shows good agreement with simulation. We again note that we expect simulation to underestimate P_{RR} . The residual distances between Eq. (B5) and all 61 simulations are shown in Figure 6 (b), with none exceeding 2%.

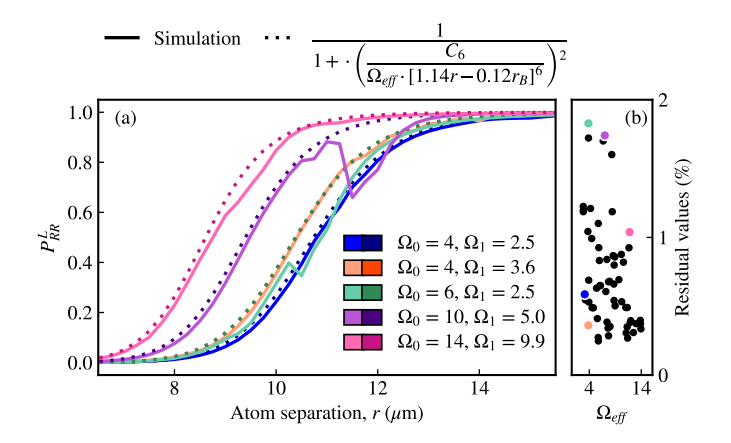


Figure 6. (a) Maximum occupation of the doubly-excited state for five simulations of local simultaneous systems and Eq. (B5). (b) For 61 of such simulations, the residual values are shown, with the 5 which correspond to the data in (a) depicted in color.

Appendix C: Description of the unit disk and disk graphs used for Section IV

We generated disk graphs G_d by first placing N atoms at random positions $\{\vec{r}_i\}_{i=1}^N$ and assigning each atom a random Rydberg blockade radius $\{r_{b,i}\}_{i=1}^N$, resulting in the graph G_d . From this disk graph, we constructed a corresponding unit disk graph G_{UD} by using a global Rydberg blockade radius $r_b = \frac{1}{N} \sum_i r_{b,i}$. The disk graph G_d was retained only if all of the following conditions were satisfied:

- G_d is not isomorphic to any unit disk graph derived from the same register of points.
- The MIS of G_d is the same size as the MIS of G_{UD} . This ensures both graphs have comparable difficulty in exciting the same number of atoms.
- No MIS of G_d is entirely contained within the set of all MIS solutions of G_{UD} , and vice versa.

- M. Saffman, T. G. Walker, and K. Mølmer, Reviews of modern physics 82, 2313 (2010).
- [2] L. Henriet, L. Beguin, A. Signoles, T. Lahaye, A. Browaeys, G.-O. Reymond, and C. Jurczak, Quantum 4, 327 (2020).
- [3] C. S. Adams, J. D. Pritchard, and J. P. Shaffer, Journal of Physics B: Atomic, Molecular and Optical Physics 53, 012002 (2019).
- [4] M. Saffman, I. Beterov, A. Dalal, E. Páez, and B. Sanders, Physical Review A 101, 062309 (2020).
- [5] H. Levine, A. Keesling, G. Semeghini, A. Omran, T. T. Wang, S. Ebadi, H. Bernien, M. Greiner, V. Vuletić, H. Pichler, et al., Physical review letters 123, 170503 (2019).
- [6] G. Pelegrí, A. J. Daley, and J. D. Pritchard, Quantum Science and Technology 7, 045020 (2022).
- [7] M.-T. Nguyen, J.-G. Liu, J. Wurtz, M. D. Lukin, S.-T. Wang, and H. Pichler, PRX Quantum 4, 010316 (2023).
- [8] P. Scholl, M. Schuler, H. J. Williams, A. A. Eberharter, D. Barredo, K.-N. Schymik, V. Lienhard, L.-P. Henry, T. C. Lang, T. Lahaye, et al., Nature 595, 233 (2021).
- [9] H. Weimer, M. Müller, I. Lesanovsky, P. Zoller, and H. P. Büchler, Nature Physics 6, 382 (2010).
- [10] M. Morgado and S. Whitlock, AVS Quantum Science 3 (2021).
- [11] M. D. Lukin, M. Fleischhauer, R. Cote, L. M. Duan, D. Jaksch, J. I. Cirac, and P. Zoller, Phys. Rev. Lett. 87, 037901 (2001).
- [12] E. Urban, T. A. Johnson, T. Henage, L. Isenhower, D. D. Yavuz, T. G. Walker, and M. Saffman, Nature Physics 5, 110–114 (2009).
- [13] A. Guttridge, D. K. Ruttley, A. C. Baldock, R. González-Férez, H. Sadeghpour, C. Adams, and S. L. Cornish, Physical Review Letters 131 (2023), 10.1103/physrevlett.131.013401.
- [14] T. Wilk, A. Gaëtan, C. Evellin, J. Wolters, Y. Miroshnychenko, P. Grangier, and A. Browaeys, Physical Review Letters 104 (2010), 10.1103/physrevlett.104.010502.
- [15] C. Dalyac, L. Leclerc, L. Vignoli, M. Djellabi, W. da Silva Coelho, B. Ximenez, A. Dareau, D. Dreon, V. E. Elfving, A. Signoles, L.-P. Henry, and L. Henriet, "Graph algorithms with neutral atom quantum processors," (2024), arXiv:2403.11931 [quant-ph].
- [16] L. Leclerc, C. Dalyac, P. Bendotti, R. Griset, J. Mikael, and L. Henriet, "Implementing transferable annealing protocols for combinatorial optimisation on neutral atom quantum processors: a case study on smart-charging of electric vehicles," (2024), arXiv:2411.16656 [quant-ph].
- [17] C. Dalyac, L. Henriet, E. Jeandel, W. Lechner, S. Perdrix, M. Porcheron, and M. Veshchezerova, EPJ Quantum Technology 8 (2021), 10.1140/epjqt/s40507-021-00100-3.
- [18] W. da Silva Coelho, L. Henriet, and L.-P. Henry, Physical Review A 107 (2023), 10.1103/physreva.107.032426.
- [19] S. Ebadi, A. Keesling, M. Cain, T. T. Wang, H. Levine, D. Bluvstein, G. Semeghini, A. Omran, J.-G. Liu, R. Samajdar, X.-Z. Luo, B. Nash, X. Gao, B. Barak, E. Farhi, S. Sachdev, N. Gemelke, L. Zhou, S. Choi, H. Pichler, S.-T. Wang, M. Greiner, V. Vuletić, and M. D. Lukin, Science 376, 1209-1215 (2022).
- [20] L.-P. Henry, S. Thabet, C. Dalyac, and L. Henriet, Phys. Rev. A 104, 032416 (2021).
- [21] L. Leclerc, L. Ortiz-Guitierrez, S. Grijalva, B. Albrecht, J. R. K. Cline, V. E. Elfving, A. Signoles, L. Henriet,

- G. D. Bimbo, U. A. Sheikh, M. Shah, L. Andrea, F. Ishtiaq, A. Duarte, S. Mugel, I. Caceres, M. Kurek, R. Orus, A. Seddik, O. Hammammi, H. Isselnane, and D. M'tamon, "Financial risk management on a neutral atom quantum processor," (2024), arXiv:2212.03223 [quant-ph].
- [22] M. Kornjača, H.-Y. Hu, C. Zhao, J. Wurtz, P. Weinberg, M. Hamdan, A. Zhdanov, S. H. Cantu, H. Zhou, R. A. Bravo, K. Bagnall, J. I. Basham, J. Campo, A. Choukri, R. DeAngelo, P. Frederick, D. Haines, J. Hammett, N. Hsu, M.-G. Hu, F. Huber, P. N. Jepsen, N. Jia, T. Karolyshyn, M. Kwon, J. Long, J. Lopatin, A. Lukin, T. Macrì, O. Marković, L. A. Martínez-Martínez, X. Meng, E. Ostroumov, D. Paquette, J. Robinson, P. S. Rodriguez, A. Singh, N. Sinha, H. Thoreen, N. Wan, D. Waxman-Lenz, T. Wong, K.-H. Wu, P. L. S. Lopes, Y. Boger, N. Gemelke, T. Kitagawa, A. Keesling, X. Gao, A. Bylinskii, S. F. Yelin, F. Liu, and S.-T. Wang, "Large-scale quantum reservoir learning with an analog quantum computer," (2024), arXiv:2407.02553 [quant-ph].
- [23] M. R. Garey and D. S. Johnson, J. ACM 25, 499 (1978).
- [24] A. Gaëtan, Y. Miroshnychenko, T. Wilk, A. Chotia, M. Viteau, D. Comparat, P. Pillet, A. Browaeys, and P. Grangier, Nature Physics 5, 115 (2009).
- [25] L. Béguin, A. Vernier, R. Chicireanu, T. Lahaye, and A. Browaeys, Physical Review Letters 110 (2013), 10.1103/physrevlett.110.263201.
- [26] D. Jaksch, J. I. Cirac, P. Zoller, S. L. Rolston, R. Côté, and M. D. Lukin, Phys. Rev. Lett. 85, 2208 (2000).
- [27] W. R. Inc., "Mathematica, Version 14.2," (2024), champaign, IL, 2024.
- [28] H. Breu and D. G. Kirkpatrick, Computational Geometry 9, 3 (1998).
- [29] E. Farhi, J. Goldstone, S. Gutmann, J. Lapan, A. Lund-gren, and D. Preda, Science 292, 472–475 (2001).
- [30] A. Das and B. K. Chakrabarti, Reviews of Modern Physics 80, 1061–1081 (2008).
- [31] T. Albash and D. A. Lidar, Reviews of Modern Physics 90 (2018), 10.1103/revmodphys.90.015002.
- [32] M. H. S. Amin, Physical Review Letters 102 (2009), 10.1103/physrevlett.102.220401.
- [33] H. Pichler, S.-T. Wang, L. Zhou, S. Choi, and M. D. Lukin, "Quantum optimization for maximum independent set using rydberg atom arrays," (2018), arXiv:1808.10816 [quant-ph].
- [34] P. Cazals, A. François, L. Henriet, L. Leclerc, M. Marin, Y. Naghmouchi, W. da Silva Coelho, F. Sikora, V. Vitale, R. Watrigant, M. W. Garzillo, and C. Dalyac, "Identifying hard native instances for the maximum independent set problem on neutral atoms quantum processors," (2025), arXiv:2502.04291 [quant-ph].
- [35] M.-T. Nguyen, J.-G. Liu, J. Wurtz, M. D. Lukin, S.-T. Wang, and H. Pichler, PRX Quantum 4 (2023), 10.1103/prxquantum.4.010316.
- [36] M. Lanthaler, K. Ender, C. Dlaska, and W. Lechner, "Quantum optimization with globally driven neutral atom arrays," (2024), arXiv:2410.03902 [quant-ph].
- [37] W. da Silva Coelho, M. D'Arcangelo, and L.-P. Henry, "Efficient protocol for solving combinatorial graph problems on neutral-atom quantum processors," (2022), arXiv:2207.13030 [quant-ph].
- [38] E. J. van Leeuwen, J. Van Leeuwen, et al., UU WINFI Informatica en Informatiekunde (2006).